



Numerical implementation of Detached Eddy Simulation on a passenger vehicle and some experimental correlation

Downloaded from: <https://research.chalmers.se>, 2024-07-27 07:06 UTC

Citation for the original published paper (version of record):

Sterken, L., Sebben, S., Löfdahl, L. (2016). Numerical implementation of Detached Eddy Simulation on a passenger vehicle and some experimental correlation. Journal of Fluids Engineering, Transactions of the ASME, 138(9): Art.no. 091105-. <http://dx.doi.org/10.1115/1.4033296>

N.B. When citing this work, cite the original published paper.

Numerical implementation of Detached Eddy Simulation on a passenger vehicle and some experimental correlation

L. Sterken

Chalmers University
Dept. of Applied Mechanics
Hörsalsvägen 7a
41258, Göteborg
Sweden

Volvo Car Group
Aerodynamics, 91760
40531, Göteborg
Sweden

Email: lennert.sterken@volvocars.com

S. Sebben

Chalmers University
Dept. of Applied Mechanics
Hörsalsvägen 7a
41258, Göteborg
Sweden

Volvo Car Group
Aerodynamics, 91760
40531, Göteborg
Sweden

L. Lofdahl

Chalmers University
Dept. of Applied Mechanics
Hörsalsvägen 7a
41258, Göteborg
Sweden

ABSTRACT

This study presents an implementation of Delayed Detached Eddy Simulation on a full-scale passenger vehicle for three configurations with the use of commercial software Harpoon (mesher) and Ansys Fluent (solver). The methodology aims to simulate the flow accurately around complex geometries at relevantly high Re-numbers for use in industrial applications, within an acceptable computational time. Geometric differences between the three configurations ensure significant drag changes that have a strong effect on the wake formation behind the vehicle. Therefore this paper focuses on the analysis of the base wake region.

At first, the paper evaluates the performance of the DDES, where it verifies the different operating conditions of the flow around the vehicle with respect to the DDES-definition. In a second step the numerical results are correlated with force measurements and time-averaged flow-field investigations, conducted in the Volvo Cars Aerodynamic wind tunnel. The comparison confirms a good agreement between the experiments and the simulations.

The resolved flow scales obtained by DDES give a further insight into differences in the wake flow characteristics between the configurations related to their contribution to drag.

Nomenclature

A	Frontal projected area of vehicle, m^2
C_D	Drag coefficient
C_{DES}	DES coefficient
C_{L_F}	Front-lift coefficient
C_{L_R}	Rear-lift coefficient
C_μ	Turbulent viscosity constant
CFD	Computational Fluid Dynamics
F_{res}	Total resistance force, N
F_A	Acceleration force, N
F_R	Rolling resistance force, N
F_G	Gravitational force, N
F_D	Aerodynamic drag, N
L	Vehicle length, m
NEDC	New European Driving Cycle
S_{ij}	Strain rate, 1/s
S^*	Strain rate invariant, 1/s
S_{wake}	Integrated wake area, m^2
T^*	Non-dimensionalised time
U_i, U_j	Mean velocity components, m/s
V_x, V_y, V_z	Mean velocity components, m/s
V_∞	Freestream velocity, m/s
WT	Wind tunnel
a	Vehicle acceleration, m/s^2
c_p	Pressure coefficient
$c_{p_{tot}}$	Total-pressure coefficient
d	Wall distance, m
\bar{d}	DDES length scale, m
f_d	DES limiter
f_r	Inertial coefficient
g	Gravitational acceleration, m/s^2
k_{res}	Resolved turbulent kinetic energy
k_{mod}	Modelled turbulent kinetic energy
m	Vehicle mass, kg
r_d	parameter in DES limiter
u'_i, u'_j	Velocity fluctuations, m/s
y^+	Dimensionless wall distance
α	Road inclination angle, $^\circ$
δ_{ij}	Kronecker delta
κ	Von Kármán constant
μ	Rolling resistance coefficient
ν	Kinematic viscosity, m^2/s
ν_t	Turbulent kinematic viscosity, m^2/s
ρ	Density, kg/m^3
Δ	Cell size, m

1 Introduction

Political legislation and consumer requirements for a sustainable society bring limitations in CO_2 -emissions and are setup over several years to coexist with the gradual development of new technologies. Together with the economical impact of reduced resources of carbon fuels causing increased fuel prices, vehicle manufacturers search for innovative methods to reduce the total driving resistance of the vehicle.

The total vehicle resistance can be summed by the inertial force F_A (acceleration), the rolling resistance F_R , gravity due to road elevation F_G and the aerodynamic resistance F_D , as given in Eq. 1. On a level road at a constant velocity, the drag is the largest contributor to the overall resistance at speeds above 65-70 kph [1], depending quadratically with the velocity.

$$\begin{aligned} F_{res} &= f_r m a + \mu m g \cos(\alpha) + m g \sin(\alpha) + C_D \frac{1}{2} \rho V^2 A \\ &= F_A + F_R + F_G + F_D \end{aligned} \quad (1)$$

For bluff bodies the overall drag force is mostly governed by pressure drag, created by the pressure difference between the front and rear of the body. An increase in base surface pressure would decrease the pressure deficit in the near wake. Hence the wake region behind a bluff body is an area where large improvements can be achieved. For squareback geometries, such as the Sport Utility Vehicle (SUV) investigated in this research, the near-wake region is characterized by a recirculation region with a specific length that ends at the free stagnation point. It contains a ring-type vortex, which can be seen in Fig. 1 behind a passenger vehicle. Duell [2] found that the location of the stagnation point changes as vortices within the shear layer forming the recirculation region are shed quasi-periodically into the far wake. This vortex shedding causes a pumping of the stagnation point in X-direction and is given as the main contributor to the aerodynamic drag. Furthermore he stipulated that the vortex shedding forms a pseudo-helical structure.

The study model on which the conclusions are drawn is a fundamental squareback vehicle with no wheels and a smooth underbody. Even though Fig. 1 suggests a similar process to occur in the near wake of a fully-detailed SUV, it is evident from previous research that a complete vehicle with rotating wheels and with a detailed underbody has a significant impact on the formation of the wake structures. The importance of rotating wheels on the base wake behind a passenger vehicle was shown where ground simulation and rotating wheels cause both a drag- and lift reduction. Interactions between the base wake and rear wheels cause an increased base pressure and improved underbody momentum [3]. Additionally, a smooth underbody beneficially influences the potential of the drag-reducing methods applied near the base of a vehicle. Barlow [4, 5] investigated the effect of the underbody roughness on the global forces and wake characteristics. The idea received renewed attention in PIV-measurements on a SUV-shaped model where it was stipulated that the possible mismatch in potential between small-scale and full-scale vehicles can be addressed to the difference in underbody roughness [6]. In the consideration that the vehicle used in this paper forms the research basis for rear-end investigations with respect to wake flow characteristics and related drag reduction, it is decided to smooth the underbody in order to improve the efficiency of drag-reducing techniques near the base.

The technique applied in this paper is inclined rear-end extensions as it is known to be one of the most effective methods to enhance the pressure recovery over the rear end and to decrease the wake size. Consequently the base pressure increases with a resulting drag reduction. On a fundamental squareback vehicle the concept of extensions to form a base cavity can be found in [7, 8]. Khalighi showed in a comparison of different cavity designs that inclined extensions reveal the

most promise for drag reduction. On full-scale passenger vehicles a straight base cavity was experimentally studied but the obtained drag reduction was only marginal [9]. Alternatively, the functionality of inclined rear-end extensions was proven to recover the base pressure more effectively [10, 11].

Both experiments and computations will be used to investigate the hypothesis brought forward by Duell in relation to a real vehicle with a fully-detailed geometry and rotating wheels. The global force trends between configurations will be correlated and time-averaged flow field measurements of the wake will be compared to wind tunnel results. Furthermore the drag changes will be connected to changes in the turbulent kinetic energy to complement the analysis with time-dependent information. This paper highlights more the numerical part of the overall investigation and starts with an examination of the DDES-performance and convergence criteria. In a later stage the obtained results can be used to improve the location prediction of interesting measurement regions in the experiments.

Understood from the above description is the requirement for advanced turbulence models capable of a time-dependent flow analysis around complex geometries at high Reynolds numbers with an accurate estimation of the aerodynamic forces. In addition, the methodology should remain practical for use in an industrial environment where a good balance between solution accuracy and CPU time is important. Unsteady RANS-simulations are namely inadequate to correctly predict the unsteady behaviour of the wake flow structures [12]. Contrarily, LES in its design form is too demanding for the current computer resources on complex geometries. As a possible solution to overcome this gap, hybrid RANS-LES models are constantly being developed and improved on. One of these models is the Detached-Eddy Simulation (DES) model, developed by Spalart and further improved to a delayed DES or DDES [13]. The model was shown to simulate the unsteady flow well over complex geometries with correct time dependencies of the structures [14] and where the flow is massively separated [15]. An example of the DDES approach with the Spalart-Almaras (SA) turbulence model on a full-scale vehicle can be found in [16].

2 Methodology

2.1 Geometrical overview

The investigated vehicle is a Volvo XC60 that is used as part of a research project at Volvo in base wake optimization with the purpose of drag reduction. Other papers of related investigations with the model are [17, 18]. A geometrical representation of the vehicle is given in Fig. 2. The model is fully detailed adding to the complexity of the numerical simulations. A summary of the characteristic vehicle dimensions is given in Table 1. Based on the vehicle length, the Reynolds-number is around 10^7 .

Besides the standard vehicle, two other configurations are simulated: an improved underbody configuration and an extension configuration with an extension length of 0.25m attached to the rear end. The geometrical changes to the baseline model are visible in Fig. 3(a) for the improved underbody and Fig. 3(b) for the rear-end extensions, respectively. The improved-underbody configuration consists of the removal of the heat deflector (1) and the placement of additional underbody panels (2 to 7). Additionally, the steplight feature is covered to keep attached flow over the exterior up to the spoiler edge (8). These modifications are also present in the extension configuration (9). The improved underbody can be considered as an intermediate step to feed high-energy flow into the base wake for the extensions (9) to become more effective.

All simulations are conducted with a closed-front lay-out, where the engine-bay volume is sealed off and removed from the volume mesh. The main motivation for the approach is to reduce the model complexity, mesh size and solver time. To correlate with the experiments, the test object

Property	Value	Unit
Length	4.63	[m]
Height	1.7	[m]
Width	1.85	[m]
Frontal area	2.61	[m ²]
Wheelbase	2.774	[m]

Table 1: Model dimensions

is prepared with grille covers, panels and foam to reduce the flow interaction of the engine-bay with the surrounding regions. A summary of all configurations is given in Table 2.

Name	Description
Configuration 1	Baseline
Configuration 2	Configuration 1 with improved underbody and covered steplight
Configuration 3	Configuration 2 with 0.25m extensions

Table 2: Configuration overview with description

2.2 Numerical procedure

The numerical simulations are based on the Delayed Detached Eddy Simulation (DDES) with a Spalart-Allmaras (SA) turbulence model. The basic idea behind DES is to perform as a turbulence model that acts as a subgrid-scale model in regions where the grid resolution is sufficiently fine and as a Reynolds-Average Navier-Stokes (RANS) model where the resolution is not fine enough. In a more practical sense, the model applies RANS conditions on the complete attached boundary layer whereas LES is applied in the regions of massively separated flow [13, 19]. This assumption makes the model appropriate for use on complex vehicles in an industrial environment. In the LES-region the large turbulent scales are both resolved spatially and with time, while the smaller scales are modelled. Ansys Fluent uses an implicit or grid-based filter to control the level of resolved and modelled energy [20].

The used DES-model is an adaptation of the original DES97-model through the introduction of a limiter f_d [13]. The limiter prevents the solution to switch to LES inside the boundary layer and is defined according to Eq. 2. A full description of the model can be found in [13].

$$f_d = 1 - \tanh\left([8r_d]^3\right) \quad (2)$$

where:

$$r_d = \frac{\mathbf{v}_t + \mathbf{v}}{\sqrt{U_{i,j}U_{i,j}}\kappa^2 d^2} \quad (3)$$

Eq. 3 consists of the turbulent kinematic viscosity \mathbf{v}_t , the molecular viscosity \mathbf{v} , the velocity gradient U_{ij} , the Von Kármán constant κ equal to 0.41 and the wall distance d . The molecular viscosity is defined as the ratio of the dynamic turbulent viscosity μ equal to $1.805e^{-5}$ and density ρ equal to 1.205.

Computed values of r_d correspond to 1 inside the boundary layer [SA] and decrease to 0 away from the wall. The resulting limiter f_d is consequently 1 in the LES regions and shifts smoothly to 0 in RANS mode, indicating that the boundary layer is completely modeled. The DDES-length scale \bar{d} is given in Eq. 4.

$$\bar{d} = d - f_d \max(0, d - C_{DES}\Delta) \quad (4)$$

Eq. 4 shows that the DDES-length scale is not only depended on the grid, defined by $\Delta = \max(\Delta x, \Delta y, \Delta z)$, but also on the eddy-viscosity field through the f_d -parameter. As a consequence the boundary layer is shielded from an LES infiltration and hence an unwanted grid-induced separation. The boundary layer is completely modelled using the RANS-equations of the SA turbulence model. The remaining DDES-parameter C_{DES} is kept at its default value of 0.65.

Besides the given parameters, a good indicator for the DDES-performance is the ratio of the resolved to the modelled turbulent stresses [19, 21, 22]. The resolved stresses can be directly obtained from Fluent as part of the time-statistics. Furthermore, the non-dimensional resolved turbulent kinetic energy k_{res} can be calculated with Eq. 5.

$$k_{res} = \frac{\langle u'^2 + v'^2 + w'^2 \rangle}{2U_\infty^2} \quad (5)$$

In DES-simulations the modelled Reynolds stresses require an additional calculation based on the Boussinesq hypothesis, given in Eq. 6 [19].

$$\overline{u'_i u'_j}_{mod} = \frac{2}{3} \delta_{ij} k_{mod} U_\infty^2 - \mathbf{v}_t \left(\frac{\delta U_i}{\delta x_j} + \frac{\delta U_j}{\delta x_i} \right) \quad (6)$$

with δ_{ij} the delta kronecker, k_{mod} the modelled turbulent kinetic energy, \mathbf{v}_t the turbulent kinematic viscosity and U_i and U_j the mean flow velocities.

The modelled turbulent kinetic energy k_{mod} is approximated in the SA-model with Eq. 7.

$$k_{mod} = \frac{\mathbf{v}_t S^*}{U_\infty^2 \sqrt{C_\mu}} \quad (7)$$

$$S^* = \sqrt{2S_{ij}S_{ij}}$$

where ν_t is the turbulent kinematic viscosity, S^* is the strain rate invariant and C_μ the turbulent viscosity constant equal to 0.09.

An initialization of the DDES-simulations is performed with a steady-state flow field solution. The RANS-simulation employs the realizable k- ϵ turbulence model with enhanced wall functions. Except for the different wall-function setting, the RANS simulations follow the default procedure at the Volvo Car Group. A more detailed description of the RANS approach can be found in [23, 24].

The unsteady simulations apply a dual time-iteration approach whereby the inner iterations are solved with the SIMPLEC scheme for the pressure-velocity coupling, as is recommended [25]. The time discretization is based on a second-order implicit scheme, whereas the momentum discretization is a second-order linear upwind scheme for stability during the initial phase, where after it is switched to a bounded central-differencing scheme to minimize the numerical dissipation during the time-averaging phase.

The computational grid is created with the software Harpoon 5.0b4 and the mesh is hexahedral dominated. Near the surface 5 to 7 prism layers, depending on the location on the vehicle, are generated to control the y^+ value at the surface. The first-cell prism layer height is kept at $y=0.6$ to give a $y^+ = 20$ [22]. While developing the volume mesh attention is paid to the near-geometry and vehicle-wake resolution to adequately capture the turbulent stresses. In particular the underbody region has shown to be sensitive to the chosen resolution where a too coarse cell size has revealed to be susceptible to the wheel wakes entering the underbody with a significant impact on the lift forces. Therefore all simulations are prepared with an additional underbody refinement. The total mesh size was around 140 to 170 million cells and the computational time was in average 500 000 CPUh.

Overall, the computational domain has a size of 50x9x10m in length, width and height respectively. The vehicle was positioned in the domain according to the distances shown in Fig. 4. The distance from the model to the inlet and to the outlet is 3L and 6L, respectively, with L the vehicle length.

The inlet in a steady-state setup has a uniform velocity distribution with a magnitude of 100 kph, a low turbulence intensity of 0.1% that matches the wind tunnel conditions and a viscosity ratio of 200. In an unsteady setup, the turbulence viscosity ratio is reduced to 10. The outlet is defined as a pressure outlet. The sides and roof of the box-shaped wind tunnel are considered a symmetry. The ground and wheels were given a moving boundary condition, with a translational velocity for the ground and a rotational velocity for the wheels. Even though unsteady simulations give the possibility to use sliding meshes for the wheels and fans, the simulations in this paper apply an MRF-methodology, taken directly from the steady-state approach [24, 26].

2.3 Experimental set-up

The measurements are conducted in the Volvo Cars Aerodynamic wind tunnel. It is a closed-circuit wind tunnel and it has a slotted-wall test section with a $27m^2$ cross-section. In 2006, a moving-ground system, provided by MTS Systems, was installed with boundary layer control. The boundary layer in the test section is controlled by a combination of scoop, suction and tangential blowing. An overview of the test section with the boundary layer control lay-out can be seen in Fig. 5. More information about the test section with the installed moving-ground system and balance system can be found in Sternéus [27].

The balance system measures the forces with a sampling rate of 20Hz for duration of 30s. On regular time intervals, Volvo Cars performs an uncertainty analysis of the balance system. The same vehicle is placed in the wind tunnel whereby the forces are measured at a velocity of 140kph.

Test conditions	ΔC_D	ΔC_{L_F}	ΔC_{L_R}
Repeatability within same test	0.001	0.001	0.005
Repeatability on different occasions	0.003	0.004	0.008

Table 3: Repeatability on the global forces of the Volvo Cars Aerodynamic Wind Tunnel at 140kph [according to EA04/2]

Table 3 shows the force differences measured by the balance for measurements within the same test and measurements on different occasions. It can be observed that the drag- and front-lift coefficients are of the same order, while the rear-lift coefficient is larger. The natural unsteadiness of the flow in the wake behind the vehicle can explain this behaviour. This analysis is conducted based on the European co-operation for Accreditation EA 4/02.

As a first step in the experimental analysis surface pressure measurements are taken around the base area of the vehicle. A total of 184 pressures are with quick-connectors mounted onto three 64-port PSI ESP pressure scanners. The pressure scanners are connected with the PSI 8400 Data Acquisition System through an SDI unit, that converts the analogue signal to a digital signal. The system is set up to acquire the signal in a 20Hz sampling rate for a 30s duration. The overall system accuracy is stated by the manufacturer as less than 0.03%. [28, 29] Spades are positioned in the separated-flow region at the base of the vehicle, seen in Fig. 6(a). In locations of attached flow, openings are drilled and pressure tubes are connected from the inside of the vehicle to minimize their effect on the oncoming flow. An example at the lamps can be seen in Fig. 6(b). Other regions are the roof region near the steplight, the exterior symmetry line and the rear bumper. The bumper is chosen to be equipped with drilled openings from a practical standpoint even though flow is separated.

In a second step the wake is analysed with the use of a traversing unit with two omnidirectional pressure probes [30], seen in Fig. 6(c). The probes are capable of measuring the flow up to $\pm 160^\circ$ cone angle with an angle accuracy of 0.1% and a total-velocity accuracy of 1%. The probe arm is positioned at an angle of 45° relative to the longitudinal direction (X) in order to improve the reversed-flow measurements. The experimental planes match the numerical planes used in post-processing, seen in Fig. 7, but they are limited to the wake region behind the vehicle. The dimensions of the specific planes is given in Table 4. They are measured discretely with a 10Hz sampling rate for 3s. More information can be found in [23].

2.4 Local drag

As stated in the introduction, the geometrical modifications are focused on a reduction in drag. Drag can be visualised by adding the pressure- and shear force on the surface of the car. As a response the vehicle emits a resistance force onto the air that can be visualised with the use of the local drag parameter [31]. The expression of local drag is given in Eq. 8 and a derivation of local drag can be found in [32]. The first term represents the total-pressure losses in the flow, the second term shows the longitudinal kinetic energy losses and the third term indicates the vortical

Wake plane	Description	Dimensions in WT
Xplane	$x = 0.1m$	Width: 3m
	behind vehicle	Height: 1.8m
Yplane	$y = 0m$	Length: 3m
		Height: 1.65m
Zplane	$z = 0.747m$	Length: 3m
	above ground	Width: 2.2m

Table 4: Plane description and dimensions. In the wind tunnel the planes are limited to the wake region behind the vehicle

resistance in the flow.

$$\begin{aligned}
C_DA = & \underbrace{\iint_{S_{wake}} (1 - c_{p_{tot}}) dS}_{\text{Term I}} - \underbrace{\iint_{S_{wake}} \left(1 - \frac{V_x}{V_\infty}\right)^2 dS}_{\text{Term II}} \\
& + \underbrace{\iint_{S_{wake}} \left(\frac{V_y^2 + V_z^2}{V_\infty^2}\right) dS}_{\text{Term III}}
\end{aligned} \tag{8}$$

3 Evaluation of the DDES-performance

Fig. 8 shows the DES-limiter f_d giving information on the location of the flow in RANS mode and in LES mode. Only the region close to the surface of the vehicle and close to the ground experiences RANS mode, indicated by $f_d = 0$. The f_d is designed to prevent LES of infiltrating the boundary layer region. Consequently, a rapid transition from RANS to LES outside the boundary layer is preferred [13].

Similarly, Fig. 9 gives the viscosity ratio $\frac{\nu_t}{\nu}$ at the symmetry plane. It shows a high turbulent viscosity near the vehicle's overall surface, in the region enclosed by the wheelhouses and between the different underbody components. The wake shear layer experiences high turbulent viscosity with a clear distinct jump at the location of cell-size increase due to the near-vehicle wake refinement zone. In this paper all configuration results presented, are based on a mesh with this viscosity-ratio jump.

The level of modelled and resolved turbulent kinetic energy is visualized in Fig. 10 for the symmetry plane and a plane through the wheel centers. The flow experiences modelled regions in the same areas as described by the viscosity ratio in Figure 9. It can be confirmed that the turbulent kinetic energy is resolved for more than 80% of its total, k_{mod} and k_{res} added together, a guideline found in [19, 21, 22].

In the design of the methodology for unsteady simulations, the dependency of grid- and solver settings on the solution is taken into consideration, as changes in settings should have a minimal effect. Based on the numerical methodology description presented in Section 2.2 it can be recalled that the underbody region is sensitive to the mesh density with an impact on the global forces. In Table 5 a refinement of the underbody from 12 mm, Configuration 1, to 6 mm, Config-

uration 2, improves both the drag coefficient and the rear-lift coefficient closer to the wind tunnel measurements. Therefore the refined underbody is chosen as default in the continued steps of the mesh investigation. An extended wake refinement of 2m to encapsulate the closure region, Configuration 3, is also simulated in order to investigate the effect of a noticeable viscosity jump in the wake that can be seen in Fig. 9 and produced by the octree-based mesh generator. The results show neither distinct differences in the global forces nor in the flow field could be observed. In addition a grid study on the boundary layer resolution is conducted. The number of prism cells and expansion rate are altered to maintain a constant total prism layer height. In a first step the first prism cell height of Configuration 2 (0.6 mm) is coarsened to 1.2 mm, Configuration 4. Mostly the prediction of the rear-lift coefficient is deteriorated, with only a minor worsening in front lift and no change in drag. In a second step, a refinement of the first prism cell height to 0.3 mm is simulated. The results in global forces are close to the forces simulated in Configuration 2, but with a small differential increase in drag and rear lift. So although minor oscillations can be observed in drag and lift as a consequence of the mesh refinement, Configuration 2 is considered good enough for the purpose of the investigations and to keep the computational time affordable for industrial use.

	Configuration	ΔC_D	ΔC_{L_F}	ΔC_{L_R}
1	No UB refinement	0.013	-0.040	0.016
2	UB refinement	0.007	-0.039	0.004
3	2 + Extended wake refinement	0.006	-0.038	0.003
4	2, but first cell height 1.2 mm	0.008	-0.044	0.034
5	2, but first cell height 0.3 mm	0.011	-0.035	0.013

Table 5: ΔC_D , ΔC_{L_F} and ΔC_{L_R} for all configurations with Δ defined as CFD - WT

Fig. 11 shows the CFL-number at the symmetry plane, with $\Delta t = 0.0002s$ in Fig. 11(a) and $\Delta t = 0.0001s$ in Fig. 11(b). In the case of $\Delta t = 0.0002s$ the CFL-number is above one in the volume near the geometry. Mockett [19] shows the CFL-influence on flow separation and vorticity creation around a sphere where a too large time step causes temporal diffusion. A CFL-number above one can be acceptable when limited to the RANS-region, but general guidelines [25] advise a $CFL < 1$ in the computational domain. Therefore, an additional simulation with $\Delta t = 0.0001s$ is conducted and compared to the simulation with $\Delta t = 0.0002s$. The difference in the force coefficients is $\Delta C_D = -0.003$, $\Delta C_{L_F} = 0.001$ and $\Delta C_{L_R} = -0.001$. Hence it can be assumed from the small force difference with the smaller time step that a $\Delta t = 0.002s$ is an acceptable compromise between accuracy and lead-time for simulations in industrial use.

4 Results and discussions

4.1 Global forces

The time-history of force coefficients, C_D , C_{L_F} and C_{L_R} , for the reference configuration is given in Fig. 12(a). The time is non-dimensionalised, T^* , based on the vehicle length and the freestream velocity, see Table 1. One flow-time second corresponds to six passages, T^* , of the flow over the

vehicle. Looking at the different coefficients, the rear-lift coefficient C_{L_R} shows the longest transient behaviour (up to $T^* \sim 8.4$ or time = 1.4s) until the initial unsteady information has decayed from a steady-state to a fully time-dependent flow, almost one complete flow pass through the computational domain ($T^* \sim 10.2$ or time = 1.7s). For each of the force coefficients a running average is superimposed and starts at $T^* = 12$ (time = 2.0s) including an additional safety margin. Fig. 12(b) gives a zoomed representation of the running average on the force coefficients. For a reliable averaged value, about 3.0 seconds of integration time or $\Delta T^* = 18$ is required before the force coefficients are sufficiently averaged, most clearly seen by the running average of C_{L_R} which continues to change with more than 2 lift counts (0.002) before T^*30 (time = 5s).

The force coefficients obtained in the simulations can be compared with the wind tunnel results. In Table 6 a comparison for each configuration is given where the deltas represent the difference between the numerical force coefficients and their corresponding wind tunnel counterparts. Generally, the drag coefficient is overestimated with 7 to 11 drag counts, equivalent to 2-3% error in prediction $(CFD-WT)/WT$. The rear-lift coefficients seem to agree with the wind tunnel data, except for the configuration with rear-end extensions with a maximum deviation of 15 counts. The front-lift coefficients however are not very well predicted, even though this can be explained by the absence of the engine-bay in the simulations, which is equivalent to an equally-distributed reference pressure inside the engine-bay. In the experiments however, the engine-bay is only sealed off as good as possible. Flow leakage into the engine-bay can still take place through small openings where it creates a pressure gradient inside the engine-bay, responsible for an increase in front lift in the experiments. A percentage error-estimation is not given for the lift coefficients in Table 6 as the low absolute values would magnify a relatively small change and consequently give an incorrect impression.

Configuration	ΔC_D	%	ΔC_{L_F}	ΔC_{L_R}
Configuration 1	0.011	+3.2	-0.037	0.002
Configuration 2	0.007	+2.1	-0.039	0.004
Configuration 3	0.009	+2.8	-0.037	0.015

Table 6: ΔC_D , ΔC_{L_F} and ΔC_{L_R} for all configurations with Δ defined as CFD - WT

With the statistical error ϵ_F calculated on each force coefficient, defined by Eq. 9, a perspective of the local variation of a specific point in time to the global variance can be obtained [33].

$$\epsilon_F(i) = \frac{F_i - \bar{F}}{\sigma_F^2} \quad \text{for } F = C_D, C_{L_F}, C_{L_R} \quad (9)$$

with σ_F^2 equal to the global variance of the force coefficient.

An example of such a calculation for C_D , C_{L_F} and C_{L_R} is given in Fig. 13. The large variation visible in the transient part of the time history, $T^* < 12$, confirms the choice of $T^* = 12$ (time = 2s) as sufficient to start the time statistics.

In order to determine the duration of the integration time required for a converged solution, a closer look to the standard deviation of the force coefficients can be taken. Fig. 14 shows a

running standard deviation calculated on each of the force coefficients with a start at $T^* = 12$ (time = 2s). Fig. 14(a) shows the result whereby the standard deviation develops towards a constant value. Here, the standard deviation of C_{L_R} confirms the three seconds requirement for a reliable average. However to answer if the integration time over a specific time interval is satisfactory a suggestion can be to calculate the running standard deviation on the running average of the force coefficients, as seen in Fig. 14(b). As the time interval gets longer, more time statistics are gathered and the running standard deviation decreases to zero. This can be used to establish a threshold on which the simulation can be considered converged with a certain degree of uncertainty. This would make it similar in idea to the uncertainty of the wind tunnel. Based on the example given in Fig. 14(b) a possible uncertainty to confirm a converged solution could be $\sigma_{\bar{C}_D} < 0.002$, $\sigma_{\bar{C}_{L_F}} < 0.002$ and $\sigma_{\bar{C}_{L_R}} < 0.004$.

4.2 Mean flow investigations

A first investigation of the accuracy of the DDES-simulations is to inspect the pressure distribution on the base of the vehicle. With a steady-state simulation approach it was shown that the pressure distribution at the base didn't match the wind tunnel results [17]. Mainly, the highest pressure region was shifted towards the rear bumper as a consequence of delayed separation at the roof, typical for k- ϵ turbulence models, resulting in an increased downwash. Fig. 15 shows the time-averaged base pressure distribution of each configuration, measured in the wind tunnel (left) and simulated with the DDES approach (right). It is worth to note that the pressures measured in the wind tunnel are not corrected for blockage, thus resulting in a lower level of c_p -values. The pressure distribution between CFD and wind tunnel is well captured with a correct position of the high-pressure region on the rear windscreen. The lower c_p on the rear bumper with the rear-end extensions compared to the improved underbody configuration is predicted well in the simulations.

Additionally, pressures along the symmetry line of the vehicle have been taken. Fig. 16 shows the c_p along the symmetryline for the vehicle with improved underbody. The experimental results are compared with the steady-state (SS) and time-averaged DDES (US) pressures from the simulations. When comparing the values between the wind tunnel and CFD, the absence of a pressure correction method in the wind tunnel has to be taken into consideration. In the present case a compensation of 0.02 in c_p is appropriate for and included in the visualisations. Fig. 16(a) shows the positive shift of c_p at the roof region in the time-averaged simulation compared to the steady-state simulation. At the base the unsteady simulation predicts a higher c_p -region near the windscreen and a lower c_p at the bumper, which is more in line with the experimental result. Fig. 16(b) confirms with the use of Δc_p between the simulations and the experiments the improved match of the DDES-simulation near the base.

To look at differences in the wake, the time-averaged local drag superimposed with $c_{p_{tot}}$ -contour lines is visualized in a transverse plane 0.1m behind the vehicle and in a symmetry plane for the reference configuration in Fig. 17 and compared with wake measurements taken in the wind tunnel. Opposed to the results obtained with steady-state simulations [17], with the DDES-approach the location of the reversed flow region is predicted accordingly at the height of the rear wind screen, seen in Fig. 17(a) and Fig. 17(b). The side mirror wake and d-pillar vortices are less pronounced than with steady-state and agree better with the wind tunnel results. Fig. 17(c) and Fig. 17(d) show a good agreement in wake shape and energy recovery between CFD and wind tunnel.

Between the three configurations in the DDES-simulations, a significant drag reduction is obtained through the improved underbody, Configuration 2, and additionally the rear-end exten-

sions, Configuration 3. The respective drag reductions as well as the lift changes compared to Configuration 1 are given in Table 7. As an indication of the obtained drag reductions with respect to achievable fuel consumption savings, Hucho [34] states that for an average-sized vehicle a drag reduction of $\Delta C_D = -0.010$ is equivalent to a fuel saving of -0.03 l/km in the NEDC-cycle.

Configuration	ΔC_D	%	ΔC_{L_F}	ΔC_{L_R}
Configuration 1	-	-	-	-
Configuration 2	-0.014	-4.0	0.013	-0.024
Configuration 3	-0.025	-7.1	0.014	0.010

Table 7: ΔC_D , ΔC_{L_F} and ΔC_{L_R} for all configurations with Δ defined as Configuration - Configuration 1

Wake flow changes responsible for the drag reduction between the configurations, shown in Table 7 are investigated with time-averaged velocity streamlines in the symmetry plane behind the vehicle (left) and in a plane at $z = 0.747m$ (right), shown in Fig. 18. The presence of the ring vortex in the wake behind the vehicle is clearly visible in all configurations. The energy losses in the underbody flow in Configuration 1 cause the lower vortex in Fig. 18(a) to attach itself to the rear bumper and to increase the aerodynamic drag. The roof vortex is not as well as developed as in Configuration 2 and 3. It is unable to pull the freestream flow downwards behind the wake-closure region. Configurations 2 and 3, Fig. 18(c) and Fig. 18(e) respectively, enhance the energy recovery of the roof-spoiler flow. The extensions in Configuration 3 move the vortex core further away from the base of the vehicle, which increases the base pressure on the wind screen, as seen in Figs 15(c-f). The underbody vortex in both configurations is detached from the rear bumper with the core at a lower position, compared to Configuration 1. The vortex improves the upsweep of the high-energy underbody flow into the wake region and to more quickly reduce the wake size. The underbody vortex core of Configuration 3 is positioned closer to the lower region of the rear bumper. It is visible in lower c_p -values at the lower bumper region, Fig. 15(c-f).

The velocity streamlines in the plane at $z = 0.747m$ show a more quasi-symmetrical flow field for all configurations as the integration time of a few seconds captures more the alternating vortex shedding and less the very low-frequency symmetric pumping effect present in the wake. In Configurations 2 and 3, Fig. 18(d) and Fig. 18(f), the closure point travels more downstream compared to Configuration 1, seen in Fig. 18(b).

A difference of the time-averaged flow field and an unsteady instant of the wake behind the vehicle is shown in Fig. 19.

4.3 Turbulent flow properties

The investigation of the mean flow properties gives a good insight into the effect of the configuration changes on the base-wake flow and its relation to the observed drag reductions between the configurations, given in Table 7. However the unsteady information that is accumulated in the simulations can be used to link the drag reductions to changes in the production of turbulent kinetic energy k_t and to further enhance the understanding of the near wake, shown in Fig. 20.

In Configuration 1, Fig. 20(a), the relatively high drag comes from insufficient energy in the

underbody shear layer upon entering the wake. As a result the turbulent mixing is more dispersed over a large area with a decrease in strength. The energy deficit can be traced back to the flow separation along the underbody, producing higher levels of k_{res} . Furthermore the larger affected area interacts earlier with the ground introducing more losses in the form of friction. In contrast, the improved underbody in Configuration 2, Fig. 20(c), maintains the high-momentum flow along the underbody, responsible for a $\Delta C_D = -0.014$. The higher mean velocity surrounding the near wake results in stronger levels of turbulent kinetic energy. A further drag reduction of $\Delta C_D = -0.025$ in Configuration 3, Fig. 20(e), is obtained by the conversion of the kinetic energy to potential energy through the delayed separation from the inclined extensions. It results in a lower turbulent kinetic energy and hence a more stabilized flow in the near wake compared to Configuration 2.

To capture the turbulent kinetic energy k_{res} in a lateral direction, a plane at $z = 0.824m$ is given in Fig. 20 (right) . All three configurations experience high regions of k_{res} due to the separated flow behind the rear wheels. These high levels are sustained longer into the wake towards the centerline behind the vehicle for Configurations 2 and 3. It indicates a longer sustained mixing towards the closure region of the wake, reducing the near wake-size and hence the drag.

To get a three-dimensional picture of the high turbulent kinetic energy regions in the wake behind each configuration, an isosurface of $k_{res} = 0.06$ is shown in Fig. 21. It confirms the dominant contribution of the roof shear layer to the turbulent kinetic energy and additionally it shows high levels near the rear bumper surface behind the rear wheels. The effect of the improved underbody on an increased turbulence production into the near wake can be observed in Configurations 2 and 3.

The turbulent kinetic energy k_{res} can be divided into the three contributing normal stresses, $\overline{u'^2}$, $\overline{v'^2}$ and $\overline{w'^2}$. Fig. 22 gives an overview of the turbulent normal stresses in the symmetry plane with Configuration 1 in Fig. 22(a to c), Configuration 2 in Fig. 22(d to f) and Configuration 3 in Fig. 22(g to i). Each column represents one direction of the normal stresses. Note the difference in scale for stresses. It can be observed that the main contributor to k_{res} results from the longitudinal fluctuations $\frac{\overline{u'^2}}{\overline{U_\infty^2}}$ in the upper and lower shear layer. The closure region of the near-wake is mainly dominated by the lateral fluctuations $\frac{\overline{v'^2}}{\overline{U_\infty^2}}$. For Configuration 2 and Configuration 3 the lateral turbulent stress is significantly larger near the closure region compared to Configuration 1. It indicates that the turbulent mixing continues to occur further downstream, which helps to ensure a more rapid closure of the near-wake region and has a direct link to the observed reduction in drag. Regarding the normal stress $\frac{\overline{w'^2}}{\overline{U_\infty^2}}$, a clear presence can be seen in the roof shear layer where energy is exchanged between the vehicle wake and the surrounding air. This energy exchange is missing in the underbody shear layer due to the presence of the ground.

5 Conclusions

The present work shows the implementation of DDES to simulate the flow around a full-scale passenger vehicle at relevantly high Re-numbers. In the implementation of DDES the choice of time step and the effect of mesh density distribution on the solution is investigated with respect to grid and time dependency while considering applicability in an industrial environment.

From the force analysis it can be concluded that the rear-lift coefficient C_{L_R} is most susceptible to the initial transient behaviour of the flow that starts from a steady-state solution. Furthermore C_{L_R} needs the longest integration time until sufficient statistics with acceptable accuracy are acquired. In all simulations, a minimum of three seconds of integration time gives satisfactory results. In addition, a threshold criteria is proposed to judge whether a converged solution is obtained.

Compared to the experiments, the computed global forces are well predicted with respect to drag and rear lift. A larger deviation can be observed for the front lift, albeit explainable by the geometric differences caused by the absence of an engine-bay in the simulations.

The pumping effect of the ring vortex structure, hypothesized by Duell as main contributor to the aerodynamic resistance, is also observed on the full-scale detailed SUV in this paper. However significant contributions from sources typical of road vehicles, such as a complex underbody and rotating wheels can be noticed to the development of the wake structures altering the turbulent properties of the wake.

The detailed underbody has a significant impact on the energy convection along the underbody. Globally, the smoothed underbody applied in this paper is responsible for a drag reduction of 14 counts (0.014). In the wake the drag reduction is visible by the detachment of the underbody ring vortex away from the base surface thereby increasing the base pressure. Furthermore more energy is available to improve the entrainment of the freestream flow into the closure region of the near-wake. The improvement is represented by a lower production of turbulent kinetic energy along the underbody, which in turn causes a more concentrated region of stronger turbulent mixing in the underbody shear layer. The overall wake turbulence is also increased due to the higher obtained freestream velocities in the wake.

The improved underbody enables the inclined rear-end extensions to further decrease the air resistance with an additional 11 drag counts (25 counts in total). The extensions convert the high kinetic energy into potential energy, causing an enhanced pressure recovery and a wake size reduction. The conversion is visible in a reduction of the turbulent kinetic energy strength, when compared to the configuration with only the improved underbody.

The rotating wheels are experienced in all configurations by the strong mixing directly behind the wheelhouse close to the base surface. It emphasizes the interaction of the base wake with the rear wheels and wheelhouse wakes resulting in a base pressure increase and as such, a drag reduction when compared to stationary wheels.

Looking at the components of the turbulent kinetic energy individually, the majority of k_{res} is produced by the longitudinal component, $\overline{u'^2}$, in the shear layer. Near the closure region the lateral component, $\overline{v'^2}$, is more prominent and is the main responsible for the energy entrainment. The normal component, $\overline{w'^2}$, contributes to the mixing of the roof shear layer, but is reduced in the underbody shear layer as a consequence of the presence of the ground plane.

6 Acknowledgments

The authors would like to acknowledge the Swedish Energy Agency, FFI Energi & Miljö, for the finance of this research together with Volvo Car Group.

References

- [1] Barnard, R., 2001. Road Vehicle Aerodynamic Design, second edition ed. Mechaero Publishing, St Albans, UK.
- [2] Duell, E., and George, A., 1999. “Experimental Study of a Ground Vehicle Near Wake”. SAE Technical Papers(1999-01-0812).
- [3] Landström, C., 2011. “Passenger Car Wheel Aerodynamics”. PhD thesis, Chalmers University of Technology, Göteborg, Sweden.
- [4] Barlow, J., Guterres, R., Ranzenbach, R., and Williams, J., 1999. “Wake Structures of Rectangular Bodies with Radius Edges near a Plane Surface”. AIAA Applied Aerodynamics Conference(AIAA-99-3151).

- [5] Barlow, J., Guterres, R., and Ranzenbach, R., 1999. "Rectangular Bodies with Radiused Edges in Ground Effect". SAE Technical Papers(1999-01-0648).
- [6] Perry, A.-K., and Passmore, M., 2013. "The Impact of Underbody Roughness on Rear Wake Structures of a Squareback Vehicle". SAE Technical Papers(2013-01-0463).
- [7] Howell, J., Sims-Williams, D., Sprot, A., and Hamlin, F., 2012. "Bluff Body Drag Reduction with Ventilated Base Cavities". SAE Int. J. Passeng. Cars - Mech Syst(2012-01-0171).
- [8] Khalighi, B., 2013. "Experimental Investigation of Aerodynamic Flow over a Bluff Body in Ground Proximity with Drag Reduction Devices". Int. J. Aerodynamics, 3(4).
- [9] Irving Brown, Y., Windsor, S., and Gaylard, A., 2010. "The Effect of Base Bleed and Rear Cavities on the Drag of an SUV". SAE Technical Papers(2010-01-0512).
- [10] Cooper, K., 2005. "Truck Aerodynamics Reborn: Lessons from the Past". SAE Technical Papers(2003-01-3376).
- [11] Browand, F., Radovich, C., and Bolvin, M., 2005. "Fuel Savings by Means of Flaps Attached to the Base of a Trailer: Field Test Results". SAE Technical Papers(2005-01-1016).
- [12] Fröhlich, J., and von Terzi, D., 2008. "Hybrid LES/RANS Methods for the Simulation of Turbulent Flows". Progress in Aerospace Sciences, 44, pp. 349–377.
- [13] Spalart, P., Deck, S., Shur, M., and Squires, K., 2006. "A New Version of Detached-Eddy Simulation, Resistant to Ambiguous Grid Densities". Theor. Comput. Fluid Dyn.
- [14] Spalart, P., 2009. "Detached Eddy Simulation". Annu. Rev. Fluid Mech., 41, pp. 181–202.
- [15] Strelets, M., 2001. "Detached Eddy Simulation of Massively Separated Flows". 39th AIAA Aerospace Sciences Meeting and Exhibit.
- [16] Islam, M., Decker, F., de Villiers, E., Jackson, A., Gines, J., Grahs, T., Gitt-Gehrke, A., and Comas i Font, J., 2009. "Application of Detached-Eddy Simulation for Automotive Aerodynamics Development". SAE Technical Papers(2009-01-0333).
- [17] Sterken, L., Sebben, S., Walker, T., and Löfdahl, L., 2013. "Experimental and Numerical Investigations of the Base Wake behind an SUV". SAE Technical Papers(2013-01-0464).
- [18] Sterken, L., Sebben, S., Walker, T., and Löfdahl, L., 2014. "The Effect of Rear-End Extensions on the Aerodynamic Forces of an SUV". SAE Technical Papers(2014-01-0602).
- [19] Mockett, C., 2009. "A Comprehensive Study of Detached-Eddy-Simulation". PhD thesis, TU Berlin, Berlin, Germany.
- [20] Fluent, A., 2011. Ansys Fluent Theory Guide, release 14.0 ed.
- [21] Pope, S., 2011. Turbulent Flows, ninth edition ed. Cambridge University Press.
- [22] de Villiers, E., 2006. "The Potential of Large Eddy Simulations for the Modeling of Wall Bounded Flows". PhD thesis, Imperial College of Science, Technology and Medicine, London, UK.
- [23] Sterken, L., 2013. Analysis of the Base Wake on Passenger Vehicles. Chalmers Reproservice, Göteborg, Sweden.
- [24] Hobeika, T., Sebben, S., and Landström, C., 2013. "Investigation of the Influence of Tyre Geometry on the Aerodynamics of Passenger Cars". SAE Int. J. Passeng. Cars - Mech. Syst.(2013-01-0955).
- [25] Menter, F., 2012. Best Practise: Scale-Resolving Simulations in ANSYS CFD. Tech. rep., ANSYS Germany GmbH.
- [26] Sebben, S., and Mlinaric, P., 2008. "Investigation of the Influence of Tyre Deflection and Tyre Contact Patch on CFD Predictions of Aerodynamic Forces on a Passenger Car". MIRA International Vehicle Aerodynamics, October.
- [27] Sternéus, J., and Walker, T., 2007. "Upgrade of the Volvo Cars Aerodynamic Wind tunnel". SAE Technical Papers(2007-01-1043).
- [28] Pressure Systems, I. System 8400 High Performance Pressure Data Acquisition.

- [29] Pressure Systems, I. ESP-16HD 32HD 64HD Miniature Electronics Pressure Scanners.
- [30] Aeroprobe, C. Omniprobe manual.
- [31] Cogotti, A., 1989. "A Strategy for Optimum Surveys of Passenger-Car Flow Fields". SAE Technical Papers(890374).
- [32] Ivanic, T., and Gilliéron, P., 2005. "Aerodynamic Drag and Ways to Reduce it". Lecture Series VKI Institute.
- [33] Mockett, C., Knacke, T., and Thiele, F., 2010. Detecton of Initial Transient and Estimation of Statistical Error in Time-Resolved Turbulent Flow Data.
- [34] Schutz, T., 2013. Hucho - Aerodynamik des Automobils, sixth edition ed. Springer Vieweg, Wiesbaden, Germany.

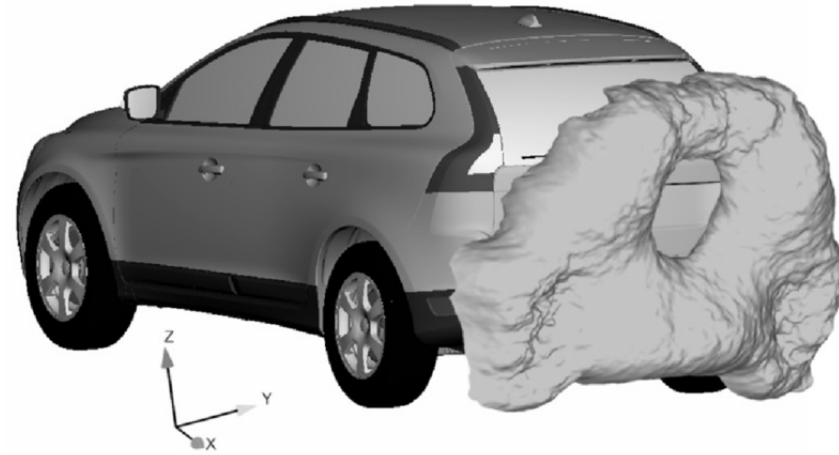
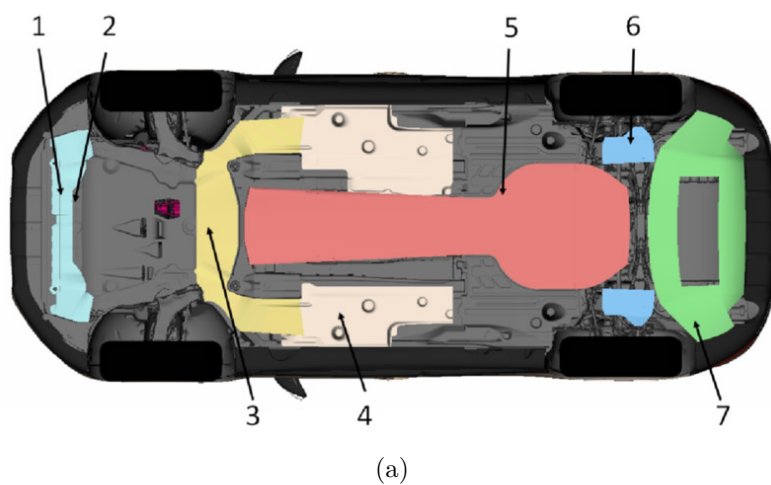


Fig. 1: Ring vortex behind squareback vehicle, created with an isosurface of $c_p = -0.22$



Fig. 2: Geometrical representation



(a)



(b)

Fig. 3: Configurational changes: (a) Improved underbody and (b) Steplight cover and 0.25m extensions

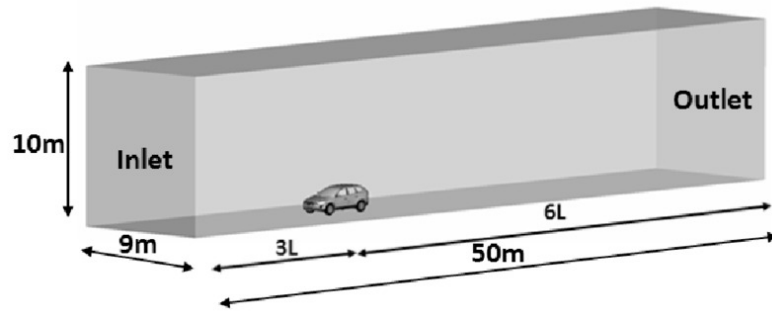


Fig. 4: Vehicle positioning in the numerical wind tunnel

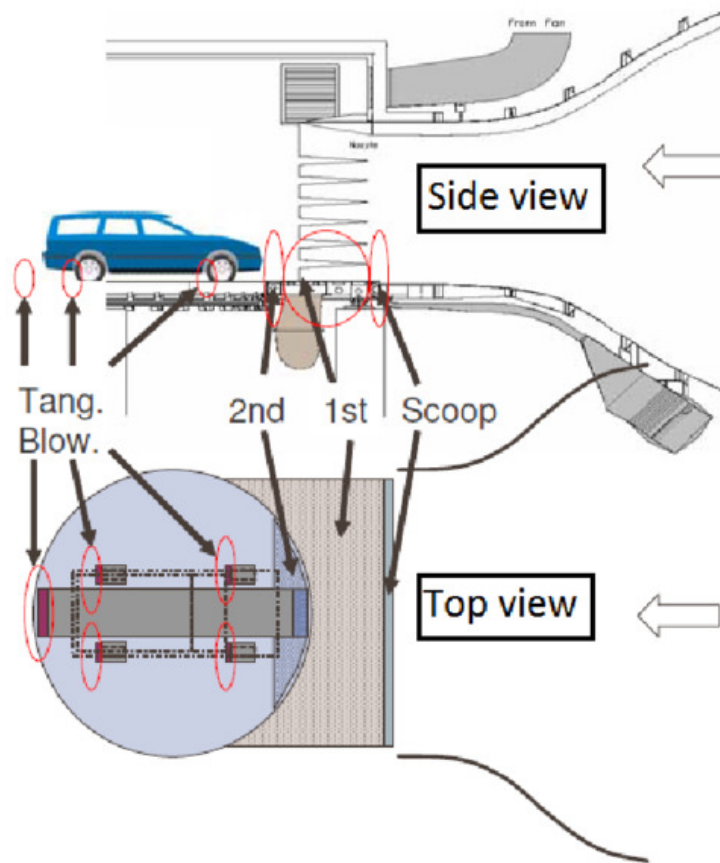
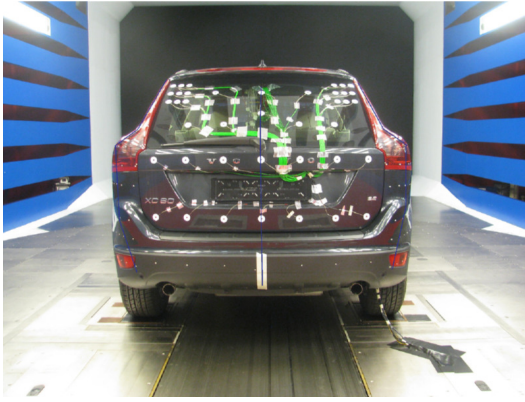


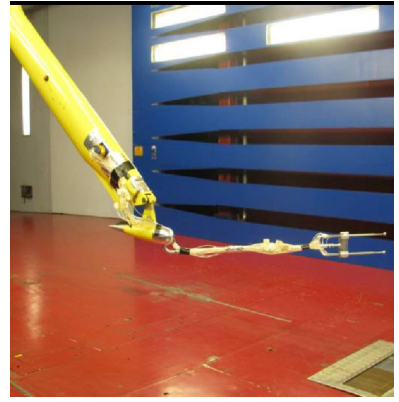
Fig. 5: Wind tunnel moving ground system [27]



(a)



(b)



(c)

Fig. 6: Overview of pressure measurements. (a) Main base region, (b) Lamp positions and (c) Traversing unit

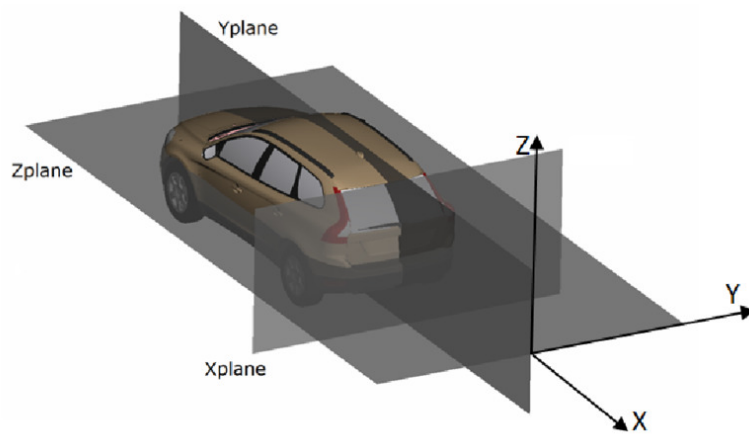


Fig. 7: Plane visualization

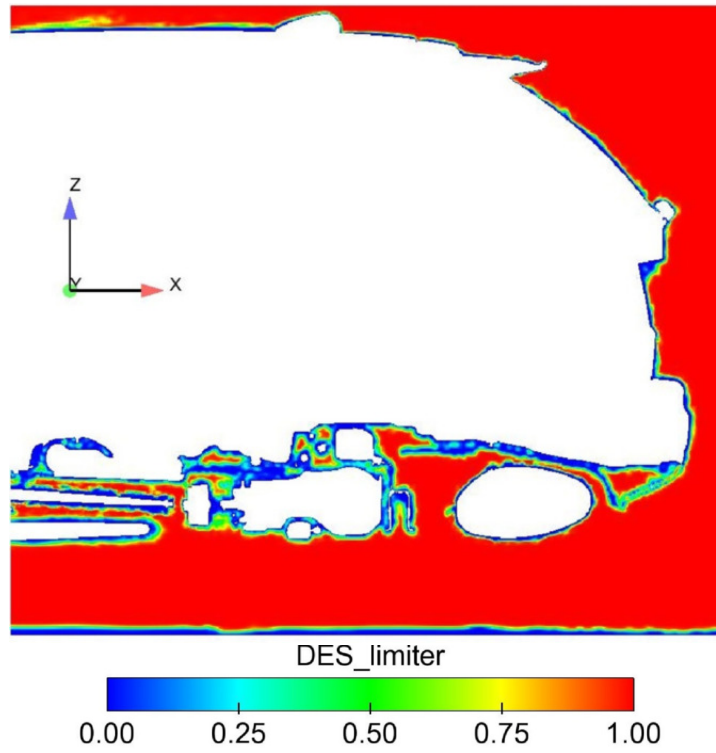


Fig. 8: DDES performance analysis: DES-limiter f_d at symmetry plane near the rear end of the vehicle

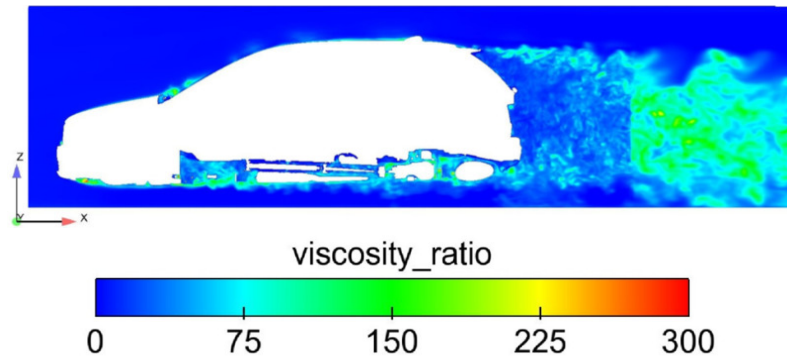


Fig. 9: DDES-performance analysis: $\frac{v_t}{v}$ at symmetry plane

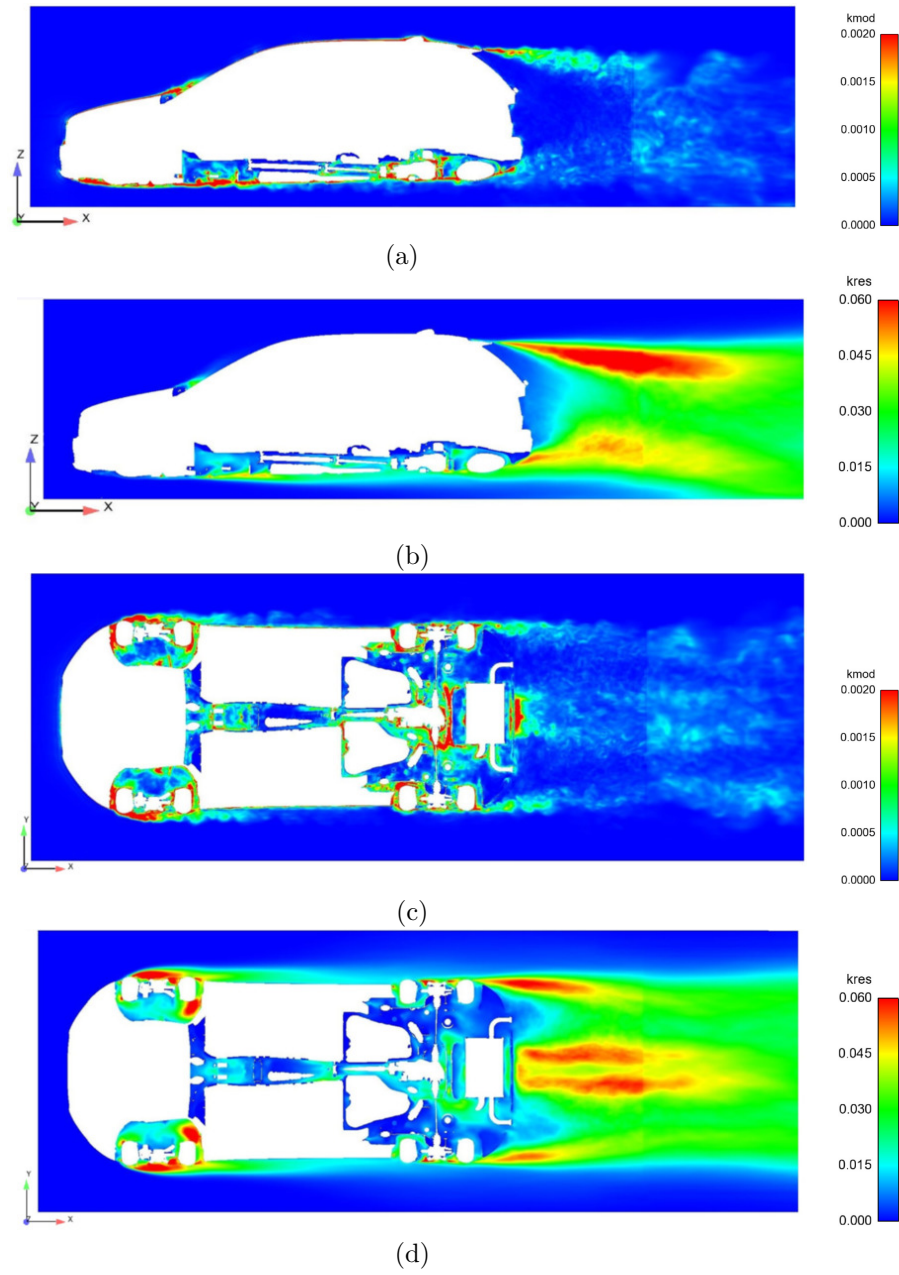
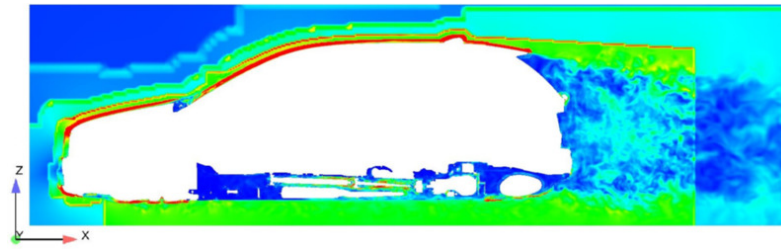
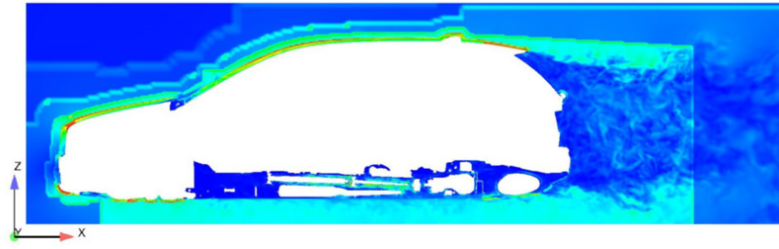
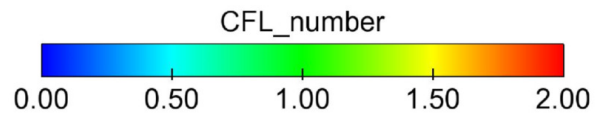


Fig. 10: DDES performance analysis: (a) k_{mod} symmetry plane, (b) k_{res} symmetry plane, (c) k_{mod} zplane through wheel centers and (d) k_{res} zplane through wheel centers



(a)



(b)

Fig. 11: CFL-number at symmetry plane: (a) $\Delta t = 0.0002$, (b) $\Delta t = 0.0001$

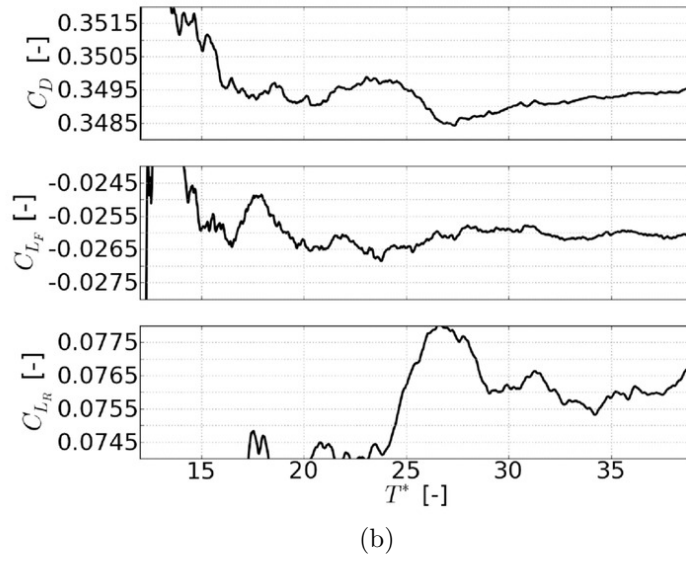
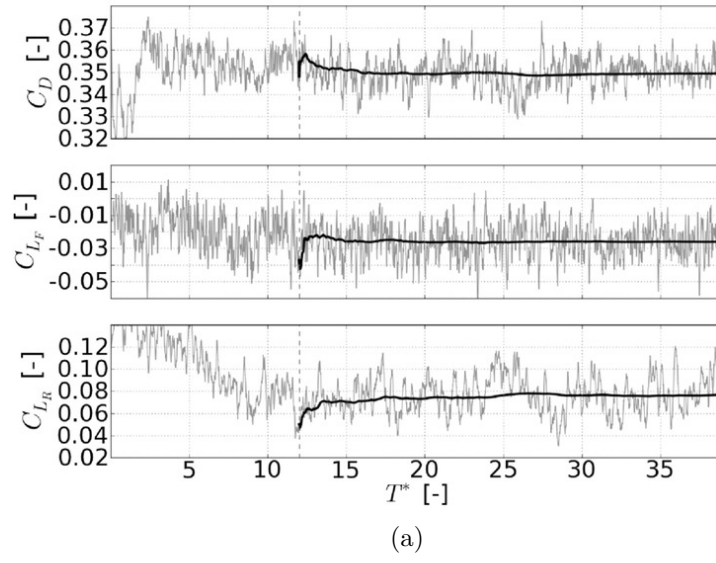


Fig. 12: Force coefficient C_D , C_{L_F} and C_{L_R} (a) Time history superimposed with running average and (b) Running average

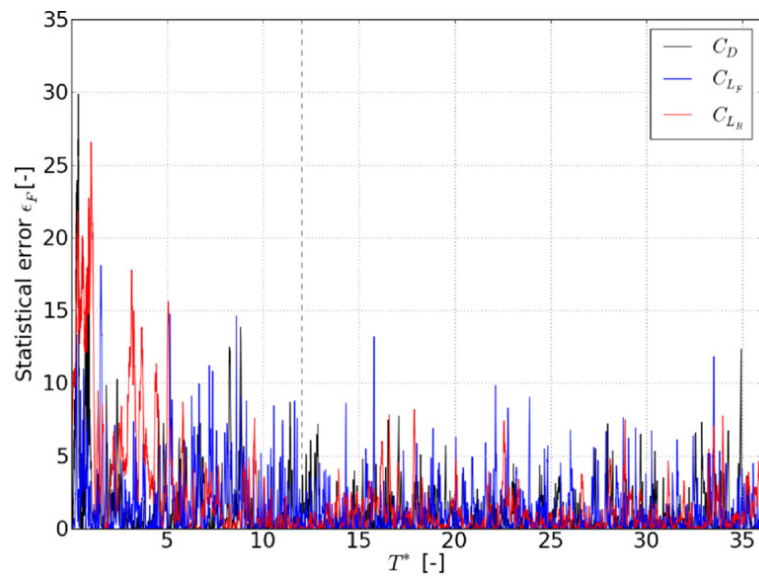


Fig. 13: Statistical error

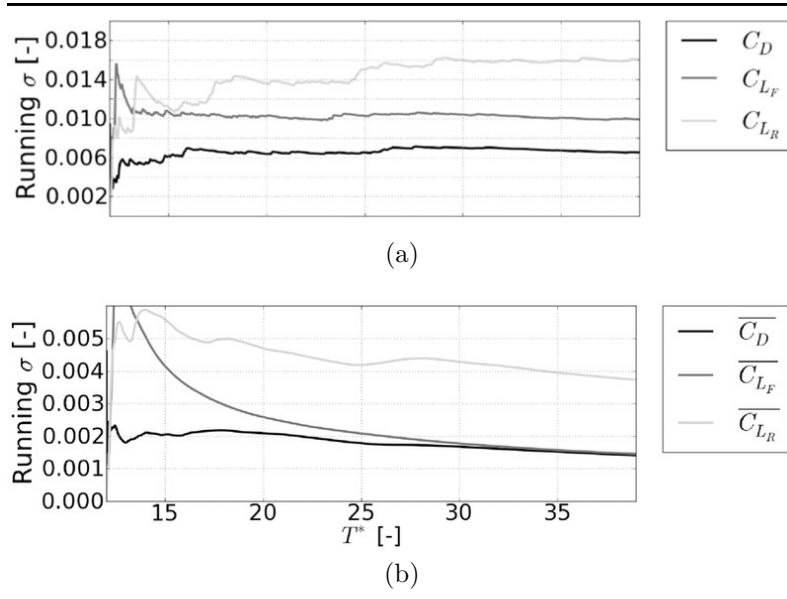


Fig. 14: Running standard deviation: (a) Force coefficients and (b) Running average of force coefficients

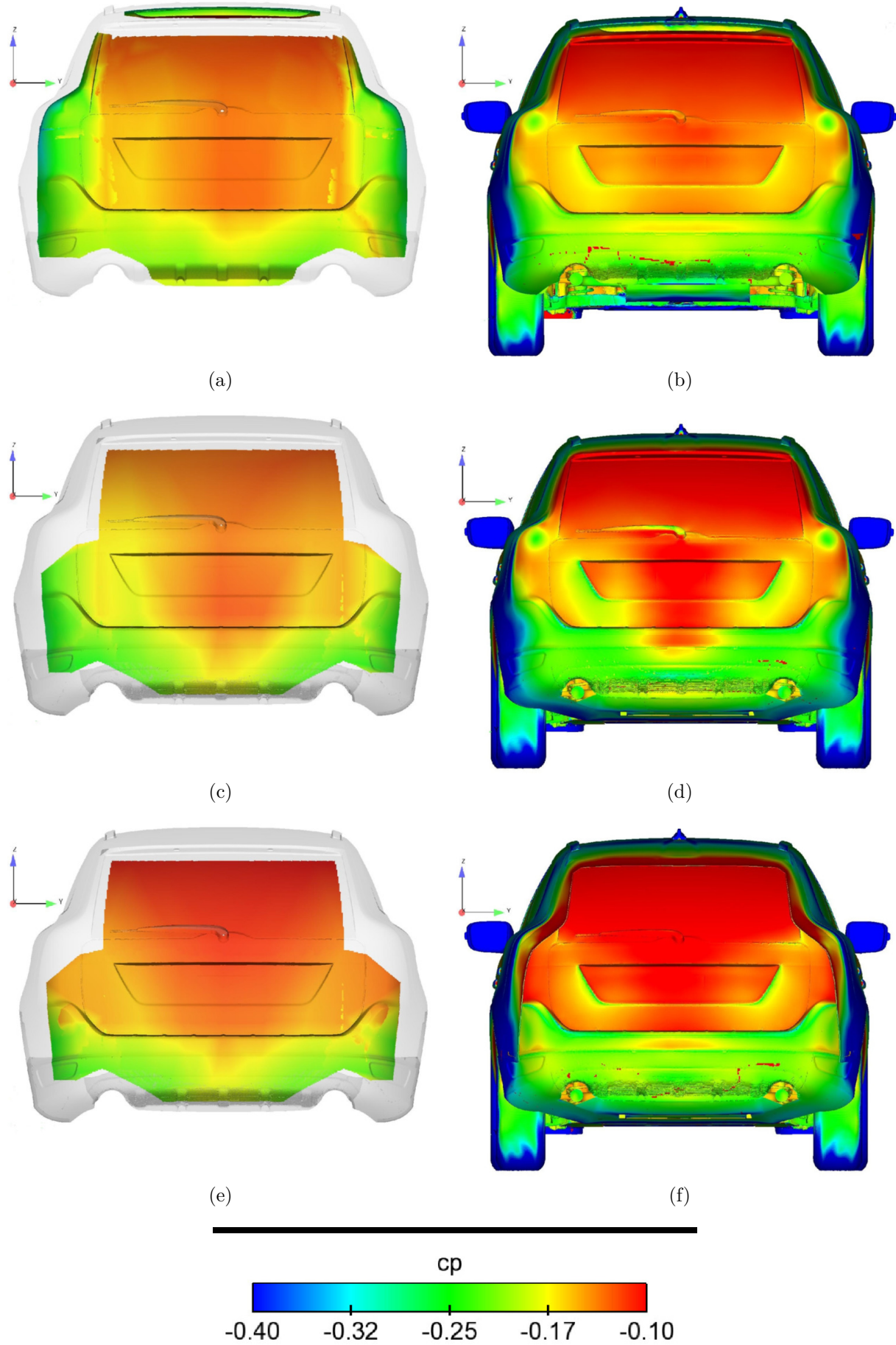
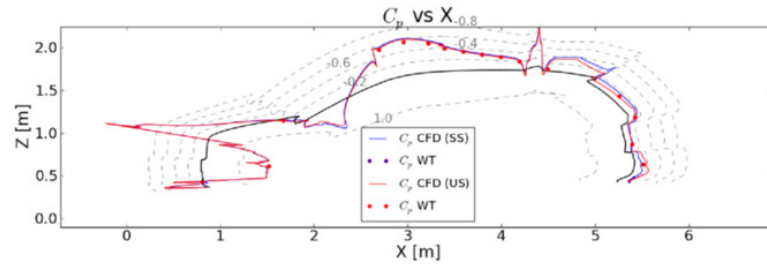
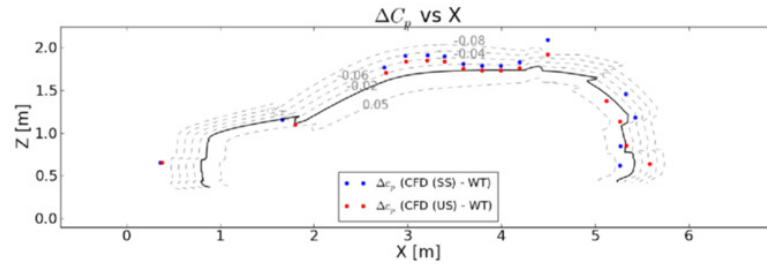


Fig. 15: Pressure distribution of base region for WT (left) and CFD (right): (a-b) Configuration 1, (c-d) Configuration 2 and (e-f) Configuration 3

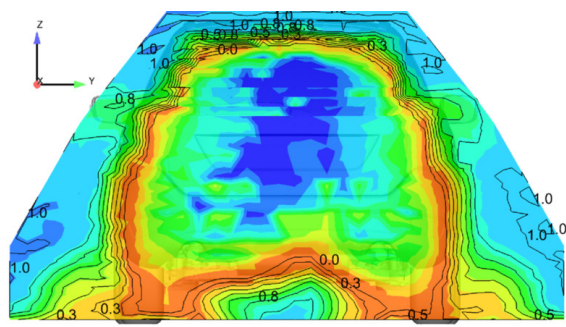


(a)

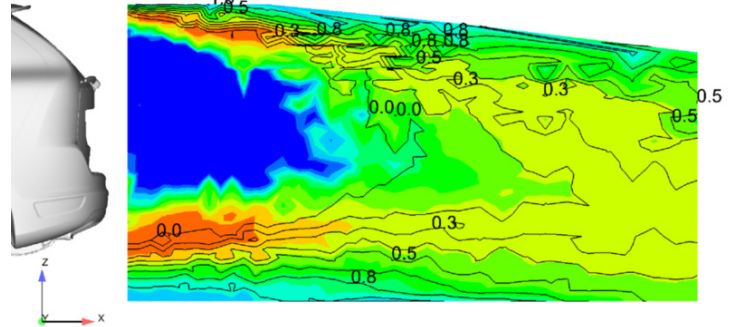


(b)

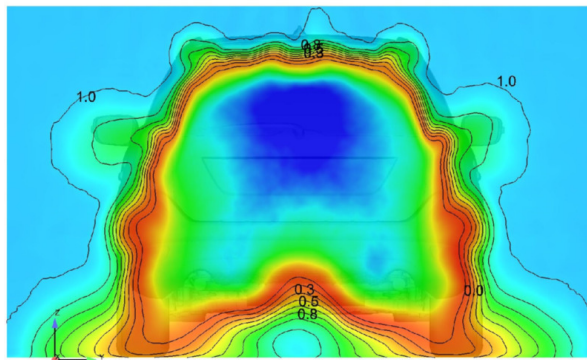
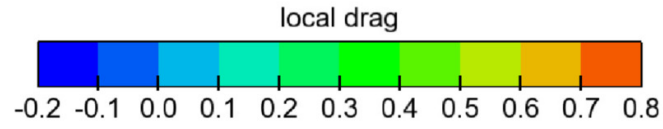
Fig. 16: Pressure distribution over symmetryline: (a) c_p and (b) Δc_p



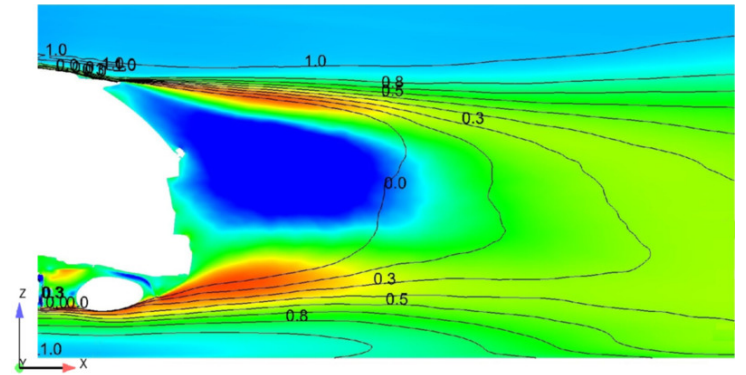
(a)



(b)



(c)



(d)

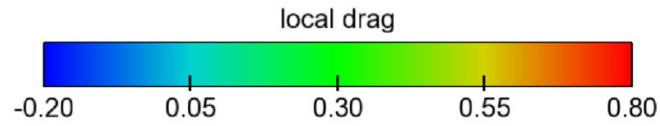
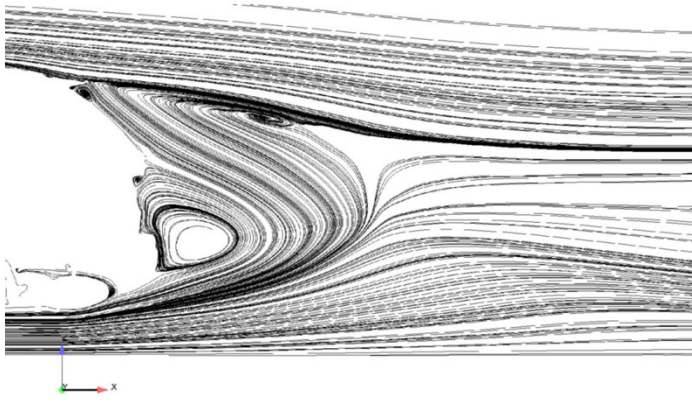
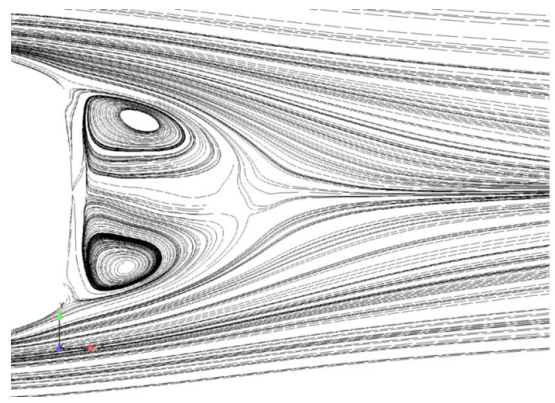


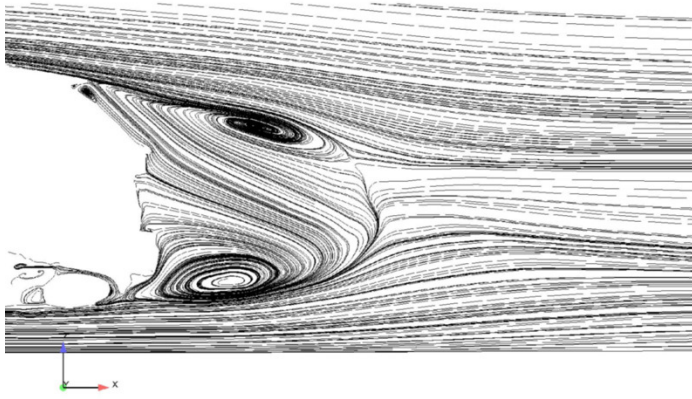
Fig. 17: Local drag superimposed with $c_{p_{tot}}$ -contour lines: (a) Transverse plane WT, (b) Symmetry plane WT, (c) Transverse plane CFD and (d) Symmetry plane CFD



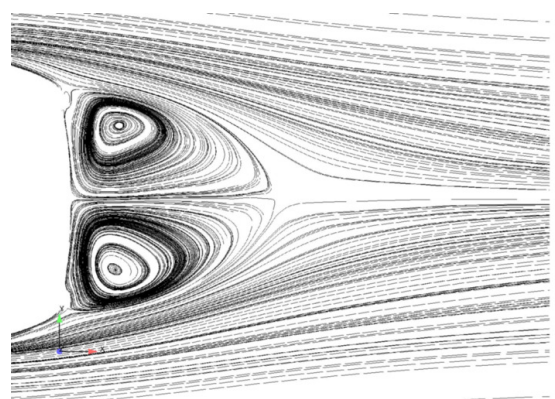
(a)



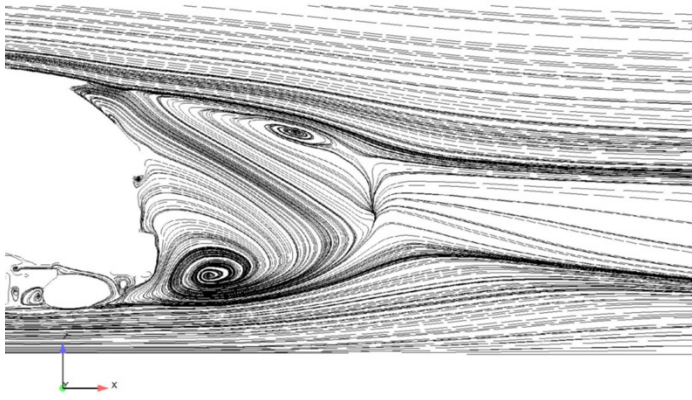
(b)



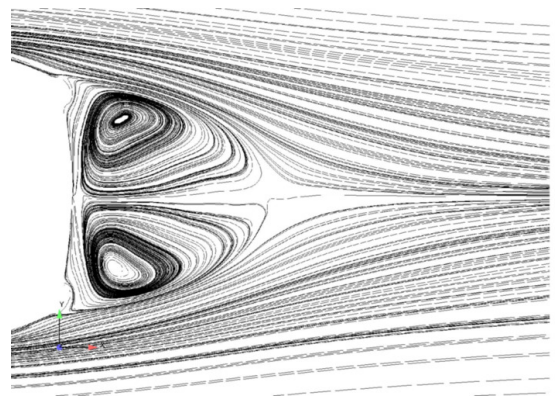
(c)



(d)

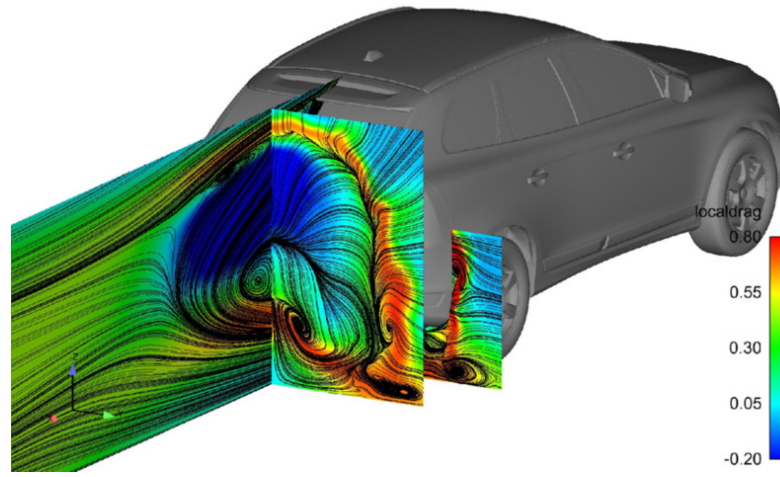


(e)

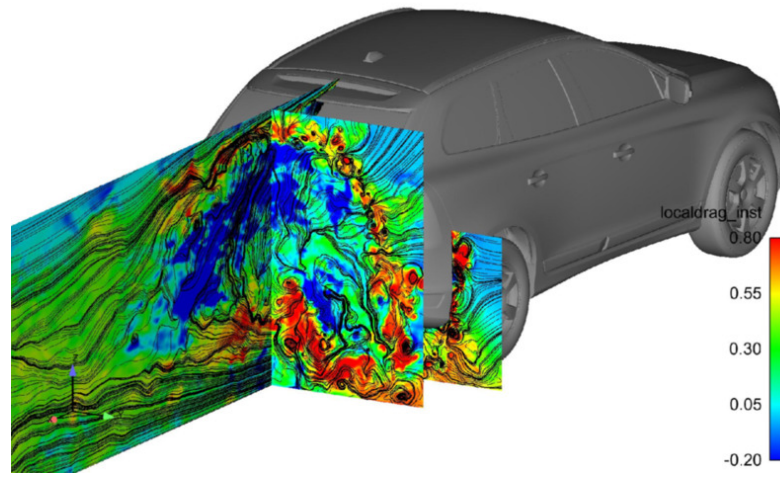


(f)

Fig. 18: Velocity streamlines in the wake behind vehicle for the symmetry plane (left) and a plane at $z = 0.747m$ (right): (a-b) Configuration 1, (c-d) Configuration 2 and (e-f) Configuration 3



(a)



(b)

Fig. 19: Local drag superimposed with streamlines for Configuration 1: (a) Time-averaged and (b) Instationary instant

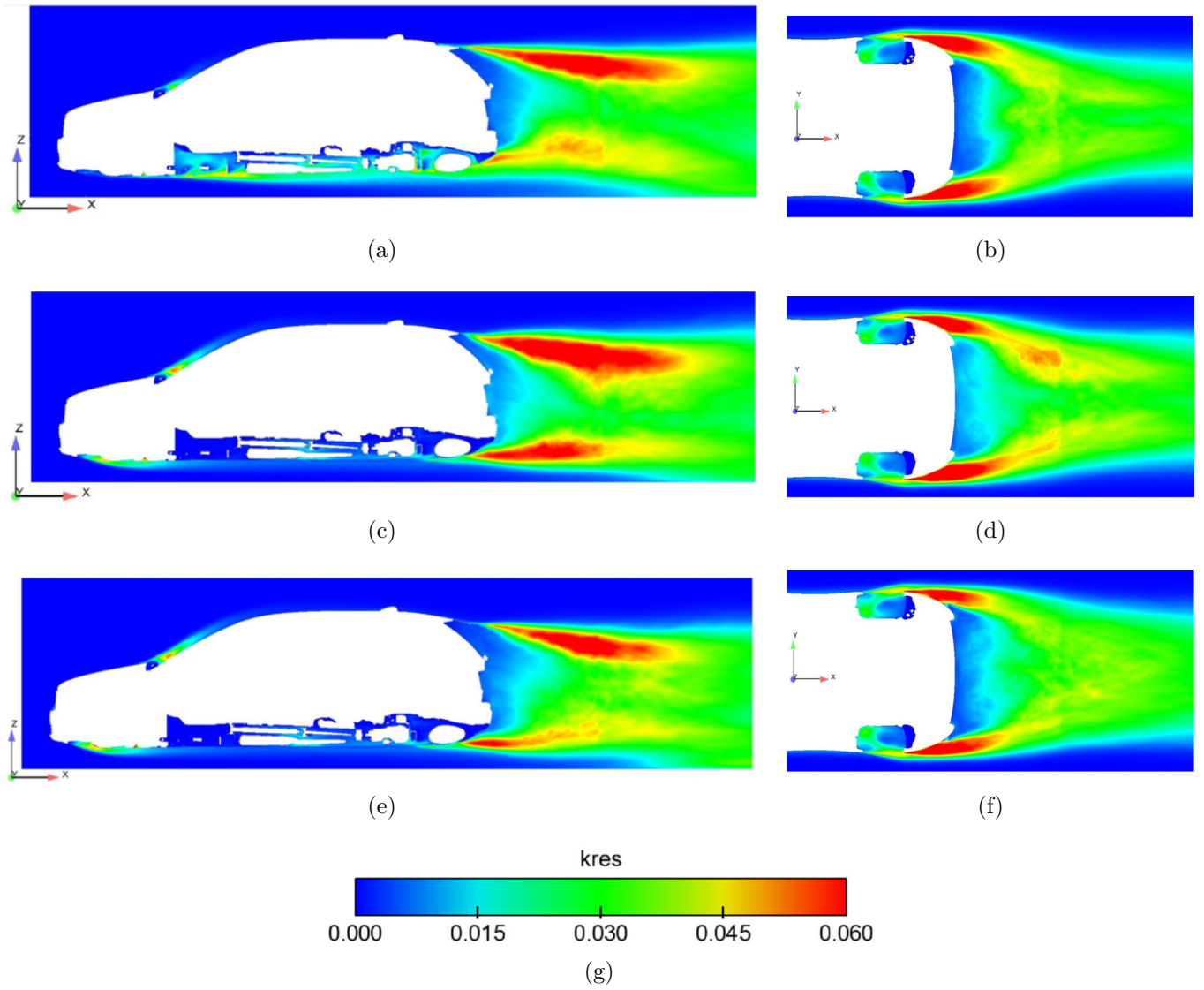
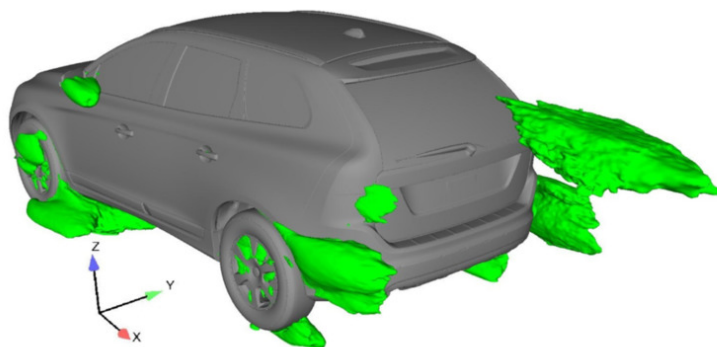
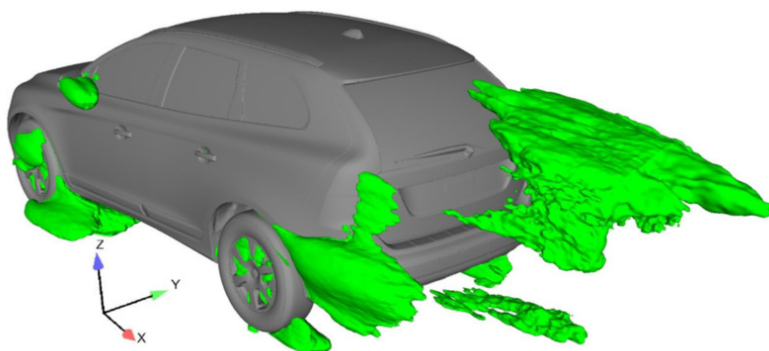


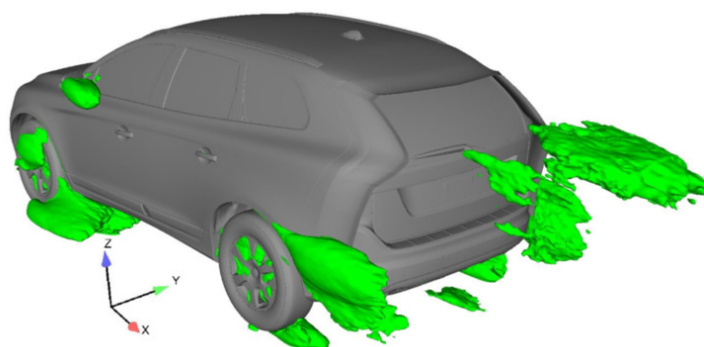
Fig. 20: k_{res} at the symmetry plane (left) and zplane at $z = 0.824m$ (right). (a-b) Reference, (c-d) Improved underbody and (e-f) Rear-end extensions



(a)



(b)



(c)

Fig. 21: Isosurface plots of $k_{res} = 0.06$: (a) Reference, (b) Improved underbody and (c) Rear-end extensions

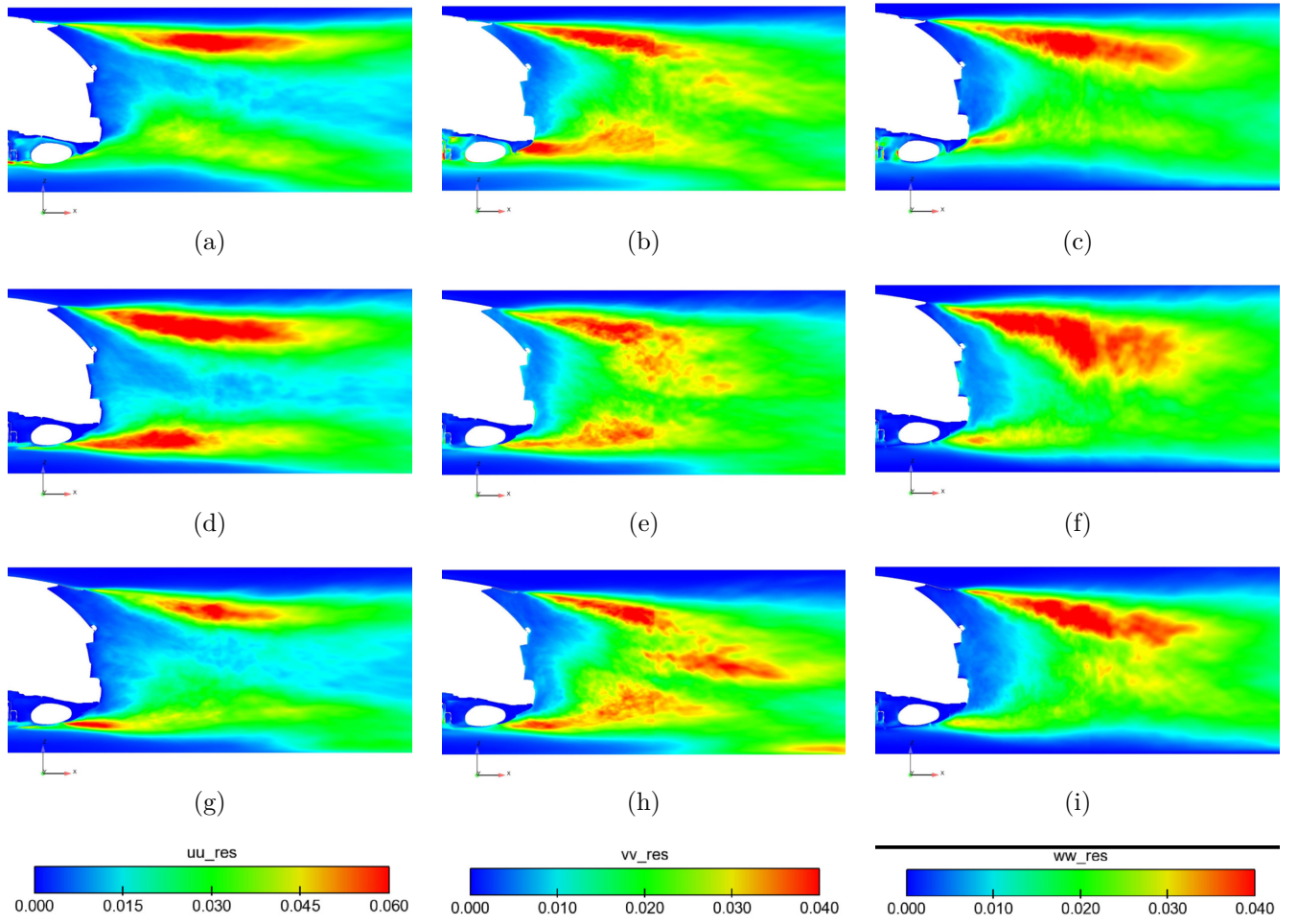


Fig. 22: Normalised turbulent stresses at the symmetry plane for $\overline{u'^2}$ (left), $\overline{v'^2}$ (middle) and $\overline{w'^2}$ (right): (a to c) Configuration 1, (d to f) Configuration 2 and (g to i) Configuration 3